International Journal of Heat and Mass Transfer 232 (2024) 125971

Contents lists available at ScienceDirect

International Journal of Heat and Mass Transfer

journal homepage: www.elsevier.com/locate/hmt

Direct numerical simulations of the transition between rotation- to buoyancy-dominated regimes in rotating Rayleigh–Bénard convection

Jiaxing Song [a,b,*], Veeraraghavan Kannan [a], Olga Shishkina [b], Xiaojue Zhu [a,**]

[a] Max Planck Institute for Solar System Research, Göttingen, 37077, Germany
[b] Max Planck Institute for Dynamics and Self-Organization, Göttingen, 37077, Germany

ARTICLE INFO

Keywords:
Rayleigh–Bénard convection
Turbulence simulation
Geostrophic flows

ABSTRACT

The flow transition between rotation-dominated and buoyancy-dominated regimes in rotating Rayleigh–Bénard convection is investigated via direct numerical simulations (DNS), for laterally periodic domains and no-slip top and bottom boundary conditions. The comprehensive transition pathway is realized by increasing the thermal driving force (Rayleigh number, Ra) over five orders of magnitude, for $Ra = 5 \times 10^6$ to 5×10^{11}, and Ekman number Ek from 1.5×10^{-6} to 5×10^{-5}, and Prandtl number $Pr = 1$. During the transition, the typical flow states, i.e., cells, Taylor columns, plumes, rotation-affected turbulence, and buoyancy-dominated turbulence are revealed. The thermal and viscous boundary layer (BL) statistics, interior temperature gradient, and scaling relations for the heat and momentum transports (reflected in the Nusselt number Nu and Reynolds number Re) as well as the convective length scale are investigated across various flow regimes. It is demonstrated that the thermal BL thickness decreases monotonically and becomes thinner than the viscous BL thickness in the buoyancy-dominated regime. Moreover, the heat and momentum transport scaling relations during the transition are shown to agree well with the recently proposed unifying transition scaling model, which is based on the balance of the thermal and viscous (Ekman) BL thicknesses (R. Ecke & O. Shishkina, Annu. Rev. Fluid Mech. 55 (2023)).

1. Introduction

Rotating thermal convection plays an essential role in the heat and momentum transport in stars and planets, in particular, in planetary atmospheres, terrestrial oceans, and also in numerous industrial processes [1–5]. Rotating Rayleigh–Bénard convection (RRBC) [6], where the fluid is heated from below and cooled from above (with a temperature difference Δ) between two parallel horizontal plates separated by a distance L, and subjected to a constant angular velocity Ω, has been served as a classical simplified model to study the fundamental underlying physics of rotation-influenced thermal convective flows [6–10].

There are basically four control parameters in a RRBC system, that is, the Rayleigh number $Ra \equiv \alpha_T g L^3 \Delta/(\kappa\nu)$ that represents the buoyancy driving force, the Prandtl number $Pr \equiv \nu/\kappa$ that denotes the diffusive properties of the fluid, the Ekman number $Ek \equiv \nu/(2\Omega L^2)$, which is the ratio of viscous force to Coriolis force and denotes the intensity of rotation, or, equivalently, the convective Rossby number $Ro_c \equiv \sqrt{g\alpha_T L\Delta}/(2\Omega L) = \sqrt{Ra/Pr}Ek$, which is the ratio of buoyancy force to Coriolis force, and the geometry aspect ratios $\Gamma \equiv d/L$ [3,6,10–12]. Here, α_T is the thermal expansion coefficient, g the gravitational acceleration, κ the thermal diffusivity, ν the kinematic viscosity of the fluid and d is the horizontal extension of the domain. The main response parameters of the convection system are the dimensionless heat transport, denoted by the Nusselt number Nu, and the convective velocity represented by the Reynolds number Re.

RRBC is rich in different flow regimes induced by the interplay between several governing forces, i.e. the Coriolis, viscous, buoyancy, and pressure-gradient forces [6,10,13,14]. Generally, for any constant rotation (even for a very strong rotation, for $Ek \leq 10^{-4}$) but gradually increasing thermal driving force (Ra), the flow will undergo a transition from a rotation-dominated regime to a buoyancy-dominated (similar to a non-rotating RBC) regime through a transitional rotation-affected regime [6,10]. Extensive research has been conducted on rapidly rotating convection and non-rotating convection separately. However, only a few studies have explored quantifying the connection between these two distinct regimes and the transition process from rotation-dominated to buoyancy-dominated convection, see e.g., [6,15]. The scaling relations for the heat transport (Nu) and momentum transport (Re) upon the control parameters Ra, Ek, and Pr are of great importance in any flow regime and they are needed for extrapolation of the

* Corresponding author at: Max Planck Institute for Dynamics and Self-Organization, Göttingen, 37077, Germany.
** Corresponding author.
E-mail addresses: jiaxing.song@ds.mpg.de (J. Song), zhux@mps.mpg.de (X. Zhu).

https://doi.org/10.1016/j.ijheatmasstransfer.2024.125971
Received 28 May 2024; Received in revised form 2 July 2024; Accepted 15 July 2024
Available online 29 July 2024

laboratory results to the real natural situations where these parameters are often extreme [5,15,16].

In the rotation-dominated regime, the governing Coriolis force is balanced by the pressure gradient; this is called the geostrophic balance [17]. Thanks to the Taylor–Proudman constraint [18,19] by the dominating Coriolis force, the flow is generally aligned in the vertical direction and organizes the flow structures with distinct convective length scales, such as cellular structures, Taylor columns, plume structures [6,10,13,20–22]. After the onset of bulk convection, the heat transport in rotationally constrained flows was shown to be throttled by the bulk dynamics and the heat transfer scaling follows $Nu \sim (Ra/Ra_c)^{\xi} = (Ra\,Ek^{4/3})^{\xi}$, with some positive ξ, where the $Ra_c \approx 8.7Ek^{-4/3}$ is the critical Rayleigh number for the onset of steady convection for fluids with $Pr \geq 0.68$ [20,21,23]. For laterally confined domains with no-slip boundaries, the wall modes prior to bulk convection [24–28] or boundary zonal flows after that [29–31] can also influence the scaling relations. In the presence of no-slip top and bottom boundaries, the formation of Ekman boundary layers (BL) and the assurance of energetic Ekman pumping substantially enhance the advection process in the thermal wind layer (or thermal BL) [21,22,32–34], resulting in the steep heat transfer scaling relation of $Nu \sim Ra^3Ek^4$ [32–38]. At very high $Ra \gtrsim 10^{12}$ and very strong rotation $Ek \lesssim 10^{-9}$ there is the geostrophic turbulence regime, where the diffusion-free heat transport scaling of $Nu \sim Ra^{3/2}Ek^2Pr^{-1/2}$ is obtained [5,6,10,16,21,38,39]. Geostrophic turbulence is chaotic, nonlinear motion of fluids characterized by decorrelated small-scale vortex structures in the bulk and thin BL thickness [14,21,22,38,40–42]. Moreover, the large-scale vortices condensate with the domain size can appear through the inverse energy cascade and lead to the cyclones and anticyclones [21,22] with higher Ra for the no-slip boundary conditions.

Beyond the rotation-dominated regime, with increasing thermal driving force, the flow goes into a rotation-affected turbulence regime, where the Coriolis and buoyancy forces are comparable [14]. The rotation-affected turbulence regime is characterized by the emission of vertical thermal plumes from the wall regions and the absence of large-scale circulations [6,43–47]. In this regime with $Pr > 1$, an optimal heat transport enhancement that results from the energetic Ekman pumping can be observed when the thicknesses of the viscous and thermal BLs are approximately equal [48,49]. How exactly scales the transition from the rotation-dominated regime to the rotation-affected regime is a topic of considerable debate. The scaling of this transition can be formulated as a relation between Ra and Ek or by defining a transition parameter $Ra\,Ek^{\zeta}$ with a proper exponent ζ that allows collapsing of the data at the transition from one regime to another, for different Ra and Ek. The observed and/or predicted transition parameters vary from $RaEk^{4/3}$ to $RaEk^2$, and is known to be dependent on Pr, Γ, and on the boundary conditions [15,32,40,47,50–52]. Hence, the exact heat transport scaling relations in this regime are also difficult to determine.

With a further increase of Ra, the flow enters the buoyancy-dominated turbulent regime, where the effect of the Coriolis forces on the flow dynamics becomes negligible. During this transition, the thicker thermal BL thickness in the rotation-dominated regime will gradually become thinner and comparable with the kinetic BL thickness in the buoyancy-dominated turbulent regime [15]. In the buoyancy-dominated turbulent regime, the flow physics and scaling features are similar to those in non-rotating turbulent convection [3,6,53,54], where the kinetic BL is determined through the shear caused by the large-scale circulations with the size of domain height and the heat transport are controlled by the thermal BL [3]. Recently, by considering the balance in the Ekman and thermal BL thicknesses, some approaches that quantify the flow states and heat transport transitions from rotation-dominated to buoyancy-dominated regimes in turbulent rotating convention have been proposed, see, e.g., [6,15].

The non-hydrostatic quasi-geostrophic equations of the reduced model have been demonstrated to provide a qualitatively correct picture of the bulk dynamics for the rotation-dominated regime [20,21,55–57]. However, the breakdown of quasi-geostrophy begins in the rotation-affected regime, which prohibits the capability of this method to simulate the flows in rotation-affected and buoyancy-dominated turbulent regimes. Given the great numerical challenge, the full exploration of the transition pathway from rotation- to buoyancy-dominated regimes in direct numerical simulations (DNS) still remains elusive.

In this study, we numerically and theoretically elucidate the comprehensive picture that describes the whole transition pathway from rapidly rotating convection to weakly rotating convection with no-slip boundary conditions. The changes in flow structures, interior temperature gradient, thermal and viscous (Ekman) BL thicknesses, kinetic energy spectra, and scaling relations for Nu and Re for various flow regimes will be examined. We will demonstrate that at constant Ek, with an increasing thermal driving force, the thermal flow structures will gradually lose their vertical coherence and change from bulk column and plumes-dominated flow into BL plume-dominated flow. As expected, the mean temperature distribution changes from a nearly conductive curve towards the isothermal fluid bulk, with gradually thinner thermal BL thickness. However, the viscous (Ekman) BL thickness remains almost constant in the rotation-dominated regime and increases slightly in the buoyancy-dominated regime. This results in a cross-over between thermal and viscous BL thicknesses during the transition pathway, which is demonstrated to agree well with the transition parameter between the rotation-dominated and weakly rotating convection proposed by [15]. The turbulent kinetic energy spectrum shows a development of a broader scaling range with an exponent close to $-5/3$. The global momentum transport is examined via the Re scaling relation derived from the classical theoretical balances of viscous–Archimedean–Coriolis (VAC) and Coriolis–inertial–Archimedean (CIA) forces [13,58–60]. The VAC-based Re scaling is shown to agree well with the data in the cellular and columnar regimes, where the characteristic convective length scales as the onset length scale $\sim Ek^{1/3}$, while the CIA-based Re scaling works well in the buoyancy-dominated turbulence regime. Moreover, the heat and momentum transport scaling relations during the transition are shown to agree well with the recently proposed unifying transition scaling model, which is based on the balance of the thermal and viscous (Ekman) BL thicknesses [6].

2. Problem formulation and computational details

The present DNS uses the Boussinesq approximation to describe RRBC of a fluid between two horizontal plates, which is rotated with a constant angular velocity Ω around the vertical axis z, under gravitational acceleration $\boldsymbol{g} = -g\boldsymbol{e}_z$ where $\boldsymbol{e}_z$ is the vertical unit vector. The chosen reference scales are the height of the domain L, the temperature difference between the plates Δ, and the characteristic free-fall velocity $U_{ff} = \sqrt{\alpha_T g L \Delta}$. Non-dimensional temperature θ, velocity $\boldsymbol{u}$, pressure p, and time t are obtained using these scales. The dimensionless governing equations for the incompressible fluid are

$$\boldsymbol{\nabla}\cdot\boldsymbol{u} = 0, \tag{1}$$

$$\frac{\partial \boldsymbol{u}}{\partial t} + \boldsymbol{u}\cdot\boldsymbol{\nabla}\boldsymbol{u} = -\boldsymbol{\nabla}p + \sqrt{\frac{Pr}{Ra}}\nabla^2\boldsymbol{u} + \theta\boldsymbol{e}_z - \frac{1}{Ek}\sqrt{\frac{Pr}{Ra}}\boldsymbol{e}_z\times\boldsymbol{u}, \tag{2}$$

$$\frac{\partial \theta}{\partial t} + \boldsymbol{u}\cdot\boldsymbol{\nabla}\theta = \frac{1}{\sqrt{RaPr}}\nabla^2\theta. \tag{3}$$

To solve the governing equations, an energy-conserving second-order finite-difference code AFiD was utilized [61–63]. The original code was updated to include a Coriolis force term in the momentum equations to account for system rotation. The code was parallelized using a two-dimensional pencil domain decomposition strategy, allowing it to effectively handle large-scale computations [62]. No-slip boundaries and constant temperature conditions at the bottom and top plates, as well as periodic boundary conditions in both horizontal directions, were applied. Based on our previous calculations [38], the

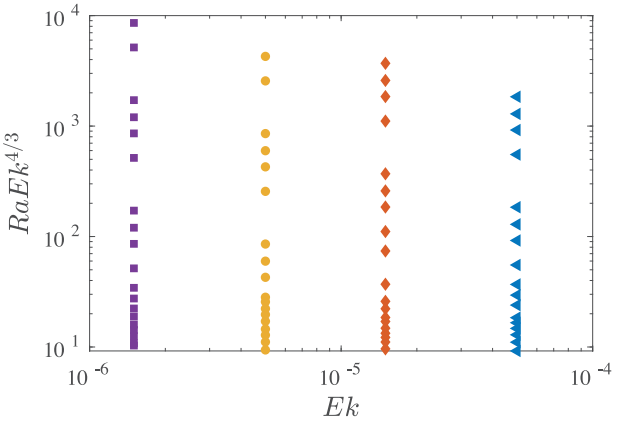

Fig. 1. Phase diagram of the present DNS on RRBC with periodic lateral boundary conditions for different Ek and Ra/Ra_c, where Ra_c is the critical value of for onset instability [7,10]. For all the simulations $Pr = 1$.

computational domain size is chosen at least ~ 20 times larger than the characteristic length scale (by the onset convection ~ $2.4Ek^{1/3}$) [14,21]. As the Chebyshev-like distribution of the grid points is applied in the wall-normal (z-) direction and a uniform distribution in the periodic (x- and y-) directions, the grid points are clustered near the bottom and top plates. In the present simulations, there are always at least 10 grid points in each thermal and viscous (Ekman) BL. For the bulk grid resolution, except for the largest simulation at $Ra = 5 \times 10^{11}, Ek = 1.5 \times 10^{-6}$, the number of the Kolmogorov lengths ($\eta \equiv \nu^{3/4}\bar{\epsilon}_u^{-1/4}$, where $\bar{\epsilon}_u$ denotes the horizontal and temporal averaged kinetic energy dissipation rate) per cell in the vertical direction Δ_z/η and the horizontal directions Δ_{xy}/η are all less than 4 that was empirically found to be acceptable by [64–66]. For this largest simulation, the number of the Kolmogorov lengths per cell in the vertical direction $\Delta_z/\eta < 3$ and the horizontal directions $\Delta_{xy}/\eta < 5$. For all studied cases, sufficiently long simulations (at least 400 free-fall time units) were performed to ensure statistically steady flow states are achieved. Moreover, ensemble averages are obtained over a time period of 200 free-fall time units after the statistically steady flow state. The convergence of the Nusselt numbers is checked for the entire domain. In this study, the maximum relative errors of the Nusselt numbers calculated by five different methods listed in the appendix were less than 1% (see Appendix for computational details). The explored parameter range in the DNS of RRBC are summarized in Fig. 1.

3. Results and discussion

As demonstrated in Fig. 2(a), for all considered Ek, after the onset of convection ($Nu > 1$), the heat transport increases dramatically with growing Ra in the rotation-dominated regime. With further increasing Ra, the convective heat transport increases mildly and gradually approaches the values of the non-rotating case, where the classical heat transport scaling of $Ra^{1/3}$ is obtained [53]. Moreover, it is found that for smaller Ek a broader range of Ra is needed to approach the scaling of non-rotating convection. This means that in strongly rotating systems, the intermediate regime of rotation-affected convection spans a wider Ra-range. Consistently, Cheng et al. [46], who used the TROCONVEX facility to study RRBC at very high $Ra \sim 10^{13}$ and low $Ek \sim 10^{-8}$, also reported that the rotation-affected regime becomes broader in Ra-range as Ek decreases in their experiments. In the rotation-dominated regime, a steep heat transfer scaling of $\sim Ra^3$ is observed for small $Ek \leq 5 \times 10^{-6}$. This steep heat transport is believed to be induced by the effective Ekman pumping effect in the presence of no-slip boundary condition, where the viscous (Ekman) BL dynamics have significant impacts on the heat transfer property of RRBC [21,34,67,68]. The full transition process from the rotation-dominated regime to the buoyancy-dominated regime can be clearly indicated by the reduced Nusselt number shown in Fig. 2(b). Specifically, with increasing supercriticality parameter $RaEk^{4/3}$, the values of Nu/Nu_0 increase monotonically from a small value close to 0.05 to ~ 1 and then saturate. Again, the range of $RaEk^{4/3}$ for the reduced Nusselt number to approach 1 gets much broader as Ek decreases. Note that in experiments [52,69] and DNS [70,71], it was demonstrated that with increasing Ra (decreasing Ek) the transition between rotation-dominated and buoyancy-dominated convection changes from gradual to sharp, due to the increasing degree of turbulence in the bulk flow (see, e.g., [72]). However, the connection between the sharp transition and the formation of the boundary flows remains unknown. In addition, further flow parameters, like Prandtl number can influence the transition. Different transition parameters are listed and discussed in [10,45], which are shown to be dependent on Pr, geometry and its aspect ratio, and also the boundary conditions. There is no overshot of the heat transfer for the parameters considered here with $Pr = 1$. Previously, it was shown that Nu exceeds Nu_0 due to energetic Ekman pumping of the thermal wind for $Pr > 1$, where the thermal BL lies within the viscous BL [6,32,48,73,74].

At a constant Ek, with increasing Ra the flow undergoes in sequence transitions to rotation-dominated, rotation-affected, and buoyancy-dominated regimes. Specifically, the corresponding typical flow states, namely, cells, convective Taylor columns, plumes, rotation-affected turbulence, and buoyancy-dominated turbulence are shown in Fig. 3. Our results on the rotation-dominated flow regimes, namely cells, convective Taylor columns and plumes obtained here are similar to previous numerical results from the asymptotically reduced model for quasigeostrophic convection [20,75,76] and from the DNS for different Pr [21,77]. The rotation-affected turbulence state also looks similar to the rotationally influenced turbulence studied in experiments [46] using TROCONVEX facility with very high $Ra \sim 10^{13}$ and low $Ek \sim 10^{-8}$. The temperature fluctuations fields demonstrate the change of flow topology: from the vertically aligned structures in the rotation-dominated regime to the local emission of plumes in rotation-affected turbulence, and eventually the breakdown of vertically coherent structures and the formation of large-scale circulations in buoyancy-dominated turbulence. During the transition, the typical convective length scale is strongly dependent on the control parameters (Ra) and the corresponding flow regimes [5,6,34,39]. Specifically, the typical convective length scale changes from the characteristic horizontal length scale which is much smaller than the domain size to the vertical length scale comparable with domain height (L). In addition, the temperature fluctuations gradually become intensive near the walls and better mixed in the bulk with increasing Ra.

The horizontal and vertical cross-sections of near-wall and bulk temperature fluctuations contour plots are shown in Fig. 4 to further characterize the flow phenomenology of the four distinct flow regimes, i.e. cells, plumes, rotation-affected turbulence, and buoyancy-dominated turbulence. The spatial characteristics of the rotation-dominated flow regimes in Fig. 4(a, e, i) and Fig. 4(b, f, j) are also consistent with previous numerical results [20,75–77]. Specifically, the temperature fluctuations near the wall regions are much stronger than in the middle height plane. In the cellular regime, the colder fluid parcels are concentrated in small regions and they are surrounded by hotter fluid, and vice versa (see Fig. 4a, e). One can observe very good vertical coherence of the temperature fluctuations in the xz-plane. In the plume regime (Fig. 4b, f, j), the flow is essentially chaotic in the bulk region, while some concentrated columnar regions still can be observed within the Ekman BL. In the view of xz-plane, most of the top-down connected hot and cold columns have lost their vertical coherences. In the rotation-affected turbulence regime, the temperature fluctuations become stronger in intensity and finer in spatial scale near the BL, but they form larger scaled areas in the middle plane because of the more sufficient mixing in the bulk region (see Fig. 4c,

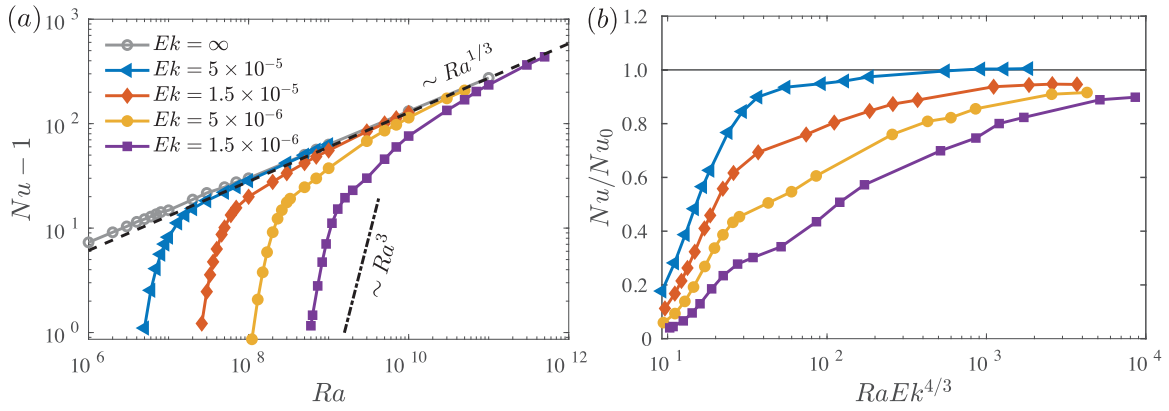

Fig. 2. (*a*) Dimensionless convective heat transport $Nu - 1$ as a function of Rayleigh number Ra, for different Ekman numbers Ek, as obtained in the DNS. The black dashed line represents the heat transfer scaling of $\sim Ra^{1/3}$ for non-rotating RBC in the classical regime, and the dash-dotted line is the steep heat transfer scaling of $\sim Ra^{3}$ for RRBC. (*b*) the Nusselt number of RRBC (Nu) divided by the Nusselt number in the non-rotating case (Nu_0) as a function of $RaEk^{4/3}$, for different Ek, where $Nu_0 = 0.067Ra^{0.33}$. (For interpretation of the references to colour in this figure legend, the reader is referred to the web version of this article.)

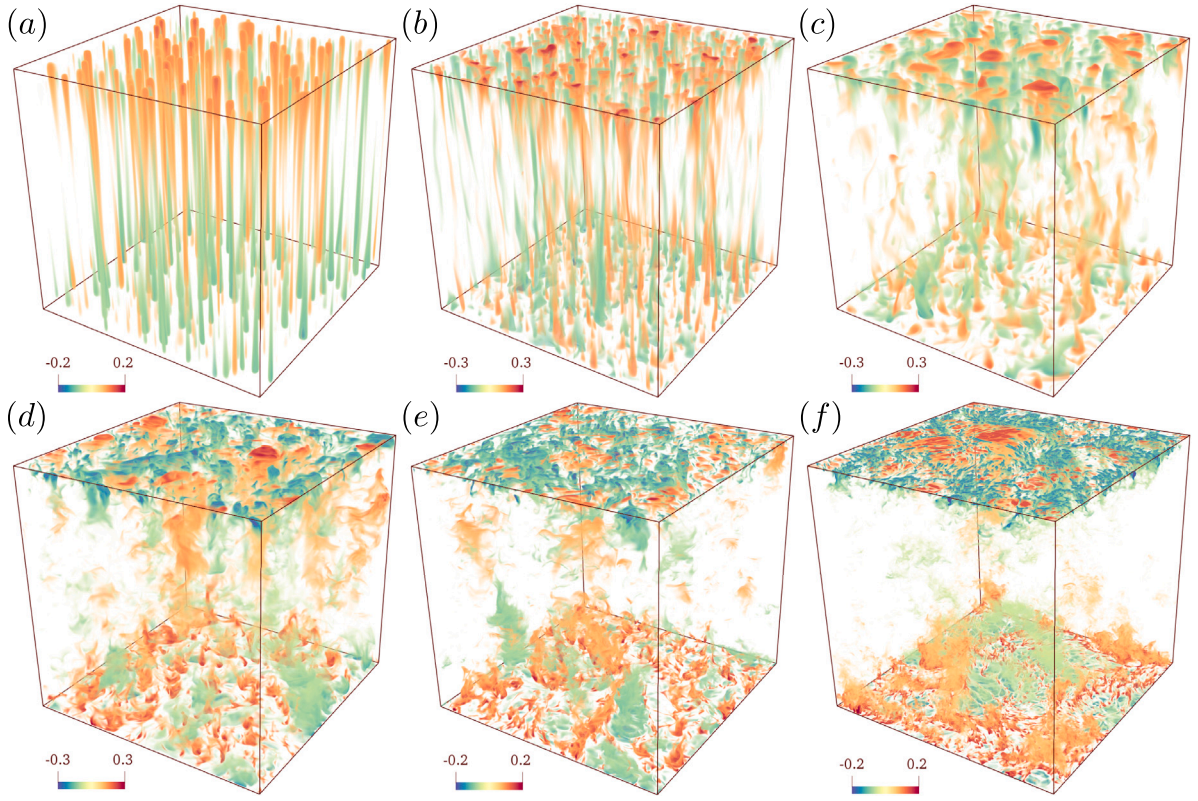

Fig. 3. Thermal fluctuations $(\theta - \langle\theta\rangle)/\Delta$ showing (*a*) cells at $RaEk^{4/3} = 12.82$; (*b*) the convective Taylor columns at $RaEk^{4/3} = 21.37$; (*c*) plumes at $RaEk^{4/3} = 85.50$; (*d*) rotation-affected turbulence at $RaEk^{4/3} = 427.49$ and (*e*) $RaEk^{4/3} = 854.99$; and (*f*) buoyancy-dominated turbulence at $RaEk^{4/3} = 4274.94$, as obtained in the DNS with no-slip boundary conditions for $Ek = 5 \times 10^{-6}$. The domains for (*a*) and (*b*) have been stretched horizontally by a factor of 0.5 for clarity. Here $\langle ... \rangle$ denotes the average in time and over horizontal cross-sections.

g). Due to the imprint of the Taylor–Proudman constraint, the induced vertical coherence can still be discerned in the *xz*-plane: the number of plumes emitted from the boundaries is almost the same as the columnar numbers in the rotation-dominated regime. As shown in Fig. 4(*d, h, l*), in the buoyancy-dominated turbulent regime, much stronger fluctuations of smaller spatial scales near the wall regions are observed. The flow pattern becomes quite similar to the flow structure with tiny detaching plumes, as it was obtained in the DNS of RBC in a cylindrical convection cell with an extremely high $Ra = 10^{13}$ at $Pr = 1$ [78]. The temperature mixes in the bulk and, intriguingly, in the vertical *xz*-plane, the flow becomes highly turbulent, and two large-scale plumes are observed, which indicates the formation of large-scale circulations in the buoyancy-dominated turbulent flow.

The gradually well-mixed temperature can also be illustrated via the mean temperature profiles across the cell, for increasing Ra, at $Ek = 5 \times 10^{-6}$ (see Fig. 5*a*). Consistent with previous studies [79], at a fixed Ekman number, an increase of Ra changes the mean temperature distribution from a nearly linear conductive state towards an isothermal fluid bulk (not fully achieved here). The mean temperature gradients near the walls increase monotonically with Ra, which implies the gradual decrease of thermal BL thickness (discussed later). The predominant

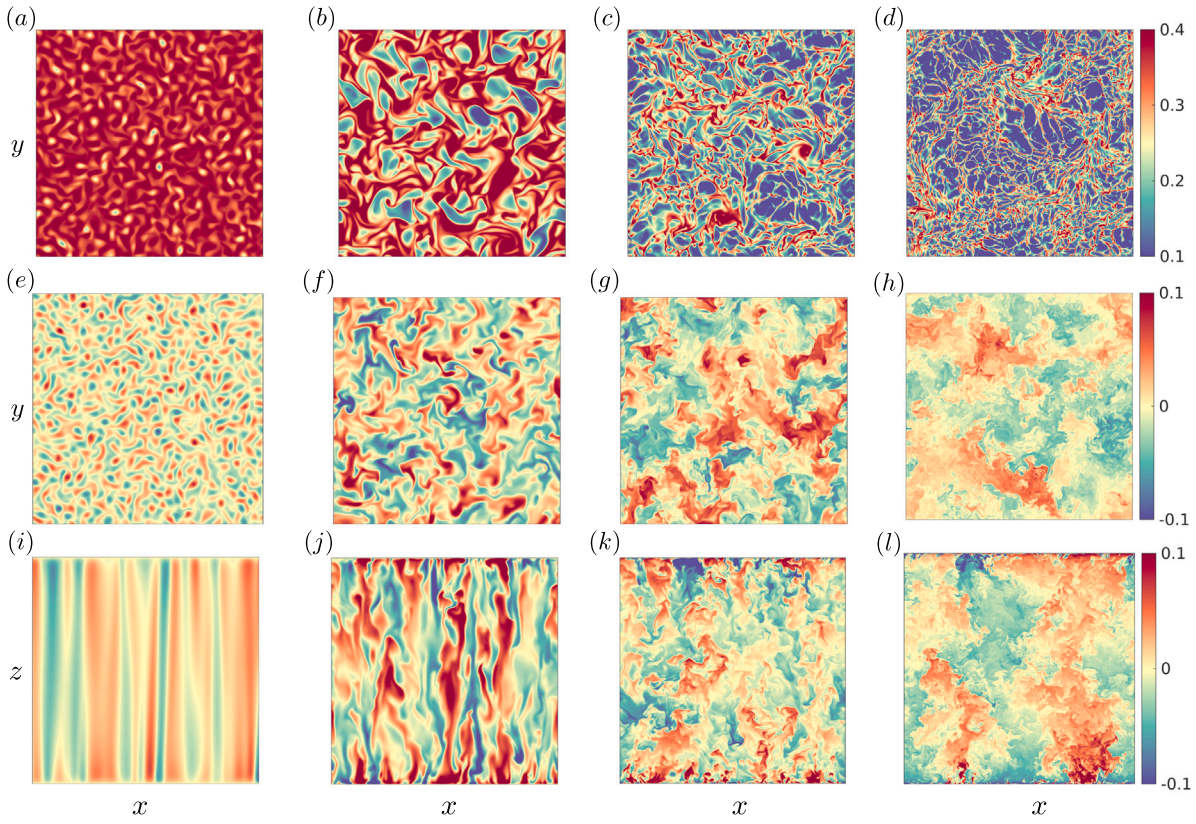

Fig. 4. Instantaneous horizontal cross sections (xy-plane) of temperature fluctuations at the edge of the bottom Ekman BL (*a–d*), midheight (*e–h*), and vertical cross sections (xz-plane) (*i–l*) for selected cases of (*a*, *e*, *i*) cells $RaEk^{4/3} = 12.82$), (*b*, *f*, *j*) plumes ($RaEk^{4/3} = 85.50$), (*c*, *g*, *k*) rotation-affected turbulence ($RaEk^{4/3} = 854.99$) and (*d*, *h*, *l*) buoyancy-dominated turbulence ($RaEk^{4/3} = 4274.94$), for $Ek = 5 \times 10^{-6}$.

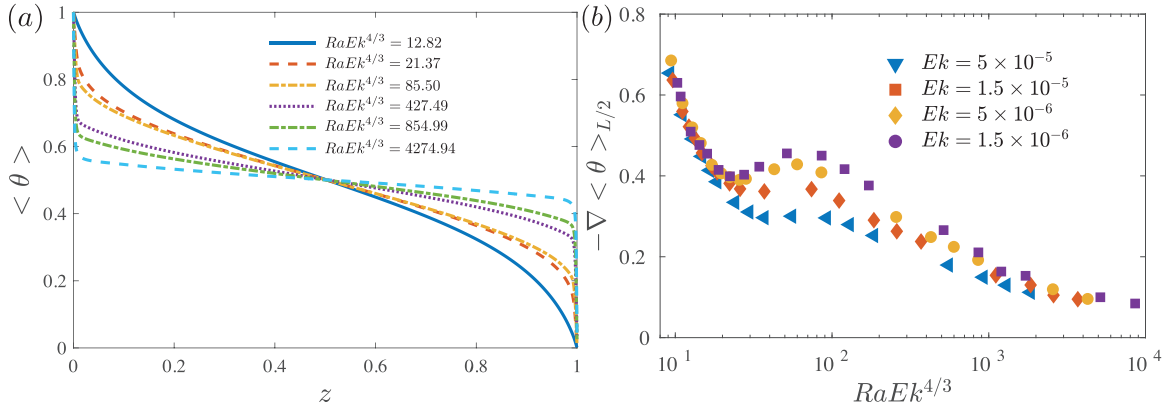

Fig. 5. (*a*) Vertical profiles of mean temperature $\langle\theta\rangle$ for different Ra (with the same values shown in Fig. 3) with a fixed Ekman number of $Ek = 5 \times 10^{-6}$. (*b*) Mean temperature gradient at mid-height as a function of $RaEk^{4/3}$ for different Ekman numbers.

interior temperature gradient maintained in the rotation-dominated regime gradually becomes flattened as the flow transitions to the buoyancy-dominated regime. The temperature gradient measured at mid-height is frequently used for determining flow regime transitions in RRBC [6,20,21,46,80]. Specifically, the mean temperature gradients at the middle height shown in Fig. 5(*b*) first decrease in the cell regime and columnar regime and then saturate or increase slightly in the plume regimes. Similar flattened mean temperature gradients, which were predicted in [20] as the transition from the plume regime to the geostrophic turbulence regime for asymptotically small Ek, were also observed in [36,46,73,81,82], for both simulations and experiments. Note that the geostrophic turbulence regime spans a distinguishing range of $RaEk^{4/3}$-values only when the thermal driving and rotating parameters reach extreme values [39]. Here, for small $Ek \leq 5 \times 10^{-6}$, a slight increase of the mean temperature gradient is obtained, which corresponds to the transition to the plume regime [75]. When $RaEk^{4/3}$ exceeds the value of $\approx$ 100, all temperature gradients decrease monotonically to about 0.1, which is relatively close to zero for the well-mixed isothermal bulk state of highly turbulent non-rotating convection. It should be noted that the mean temperature gradient shows no signs of the transition between the rotation-affected and buoyancy-dominated turbulent regimes.

Before discussing the BL statistics, we first evaluate the thermal and viscous BL thicknesses, using the frequently used approaches in RBC research [79,83,84]. Specifically, the thermal BL thickness δ_θ/L is defined by the slope method as the depth where the linear fit to the mean temperature profile near the wall intersects the linear fit to the profile at mid-depth. The viscous BL thickness δ_u/L is defined

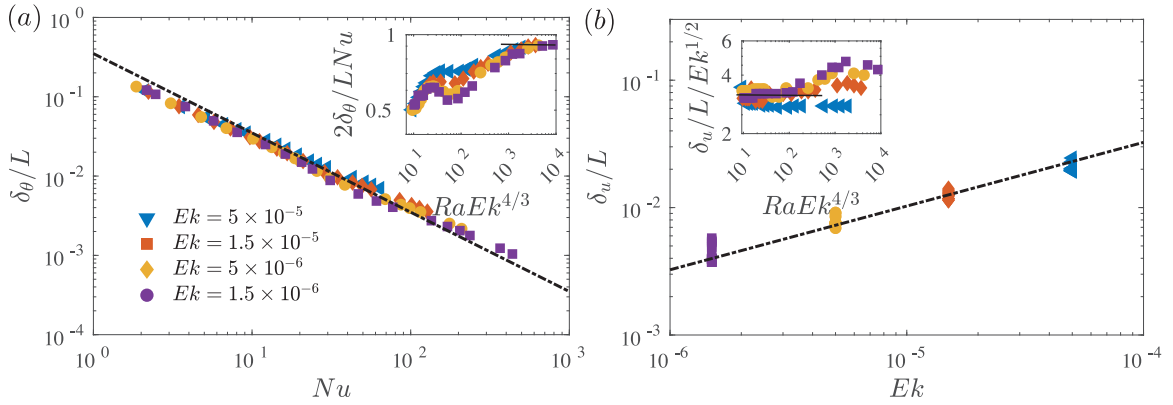

Fig. 6. (*a*) The dimensionless thermal BL thickness δ_θ/L versus Nu, for different Ek. The dash-dotted line denotes $\delta_\theta/L = 0.35Nu^{-1}$. The inset shows the compensated plot with $(2Nu)^{-1}$. (*b*) The dimensionless viscous BL thicknesses are defined by the maximum value method δ_u/L, as functions of Ek, for different Ra. The dash-dotted line denotes $\delta_u/L = 3.25Ek^{1/2}$. The inset shows the compensated plots with $Ek^{1/2}$ for δ_u as functions of $RaEk^{4/3}$, for different Ek. The symbols have the same meaning as in Fig. 2.

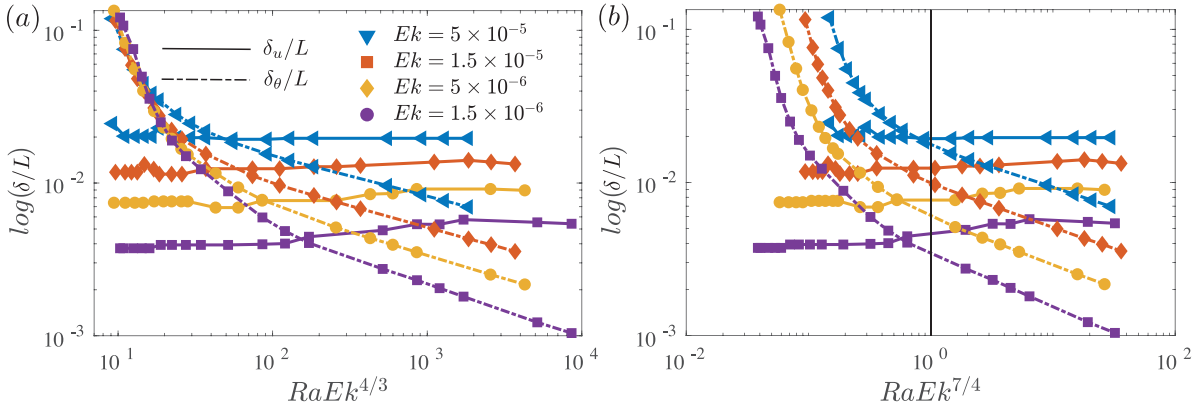

Fig. 7. The non-dimensional thermal (δ_θ/L) and viscous (δ_u/L) BL thicknesses as a functions of (*a*) the supercriticality parameter $RaEk^{4/3}$ and (*b*) the transition parameter $RaEk^{7/4}$ proposed in [15].

by the maximum values methods as the average distance from the bottom and top walls to the maximum value of $u_h = \sqrt{\langle u_x^2 + u_y^2 \rangle}$ near each wall [39]. In non-rotating RBC, the heat transport behaviour is intimately related to the BL dynamics. Specifically, relation $\delta_\theta/L \approx (2Nu)^{-1}$ is demonstrated to be valid, especially for the highly turbulent non-rotating convection [3]. As shown in Fig. 6(*a*), in RRBC, this relation does not hold well, which implies that the temperature gradient in the BL is not purely conductive, especially for the flow in the rotation-dominated regime. This has also been reported in [32]. Moreover, as shown in the inset, with increasing $RaEk^{4/3}$, in the cell and cellular regimes, the compensated value first increases and is then followed by a slight decrease in the plume regime for $Ek \leq 1.5 \times 10^{-5}$. In turn, the compensated value increases monotonically from about 0.7 to 0.9 when the flow undergoes a transition from the rotation-affected regime to the buoyancy-dominated regime. In Fig. 6(*b*), the viscous (Ekman) BL thickness is plotted versus Ek. According to the linear stability analysis [17] of steady RRBC, relation $\delta_u/L \sim 3Ek^{1/2}$ should hold close to the onset of convection. This relation can also be obtained by considering a force balance between the Coriolis force and viscous force in the limit of $Ek \to 0$ [17]. Consistent with [32,51], this scaling relation is observed in the present DNS data, especially for the rotation-dominated regime ($RaEk^{4/3} \leq 200$), as one can see in the inset plot. The compensated values get larger than 3 as the flow undergoes the transition to the rotation-affected and buoyancy-dominated regimes. This implies that buoyancy gradually changes the Ekman BL type into the kinetic BL, which is typical for non-rotating RBC, where it is mainly determined by the shear induced by the large-scale circulation [3].

As mentioned above, at constant Ek, the dimensionless thermal BL thickness δ_θ/L decreases monotonically with increasing Ra during the transition. Usually in the presence of the no-slip boundary conditions, the viscous (Ekman) BL thickness δ_u/L is thinner than the thermal one, in the rotation-dominated regime and $Pr = 1$. It is anticipated that in the rotation-affected regime, the two BL thicknesses become approximately equal [6,15,32,51]. As demonstrated in Fig. 7(*a*), indeed, δ_θ/L decreases monotonically with increasing Ra, while δ_u/L remains almost constant in the rotation-dominated regime and increases slightly in the buoyancy-dominated regime. As expected, there is a crossover between these two BL thicknesses for each Ek. Moreover, the supercriticality parameter $RaEk^{4/3}$ at the crossover point increases monotonically with decreasing Ek. Based on the heat transfer scaling relations observed in the rotation-dominated convection and non-rotating thermal convection, in [15] it was suggested that the transition parameter that separates the two regimes is $RaEk^{7/4} \sim 1$. It was demonstrated that this transition parameter matches well with their extensive experimental and numerical results, especially for the crossover point of two BL thicknesses. As expected, as demonstrated in Fig. 7(*b*), the transition points for all the considered Ek are very close to $RaEk^{7/4} \sim 1$. This implies that the $RaEk^{7/4} \sim 1$ represents quite well the crossover point between the thermal and Ekman BL thicknesses obtained from our DNS data. It should be noted that the convective Rossby number $Ro_c = Ra^{1/2}EkPr^{-1/2}$, which is the ratio of the global magnitude of the relevant buoyancy force to the Coriolis force, fails to predict this crossover. This also can be concluded based on our DNS data, as shown in Appendix (see the convective Rossby number values).

To quantify how the energy spectra change during the flow transition pathway, we calculate the turbulent kinetic energy spectra $E_{ut}(k)$ and temperature energy spectra $E_\theta(k)$ for the cells, plumes, rotation-affected and buoyancy-dominated turbulent regimes. The one-

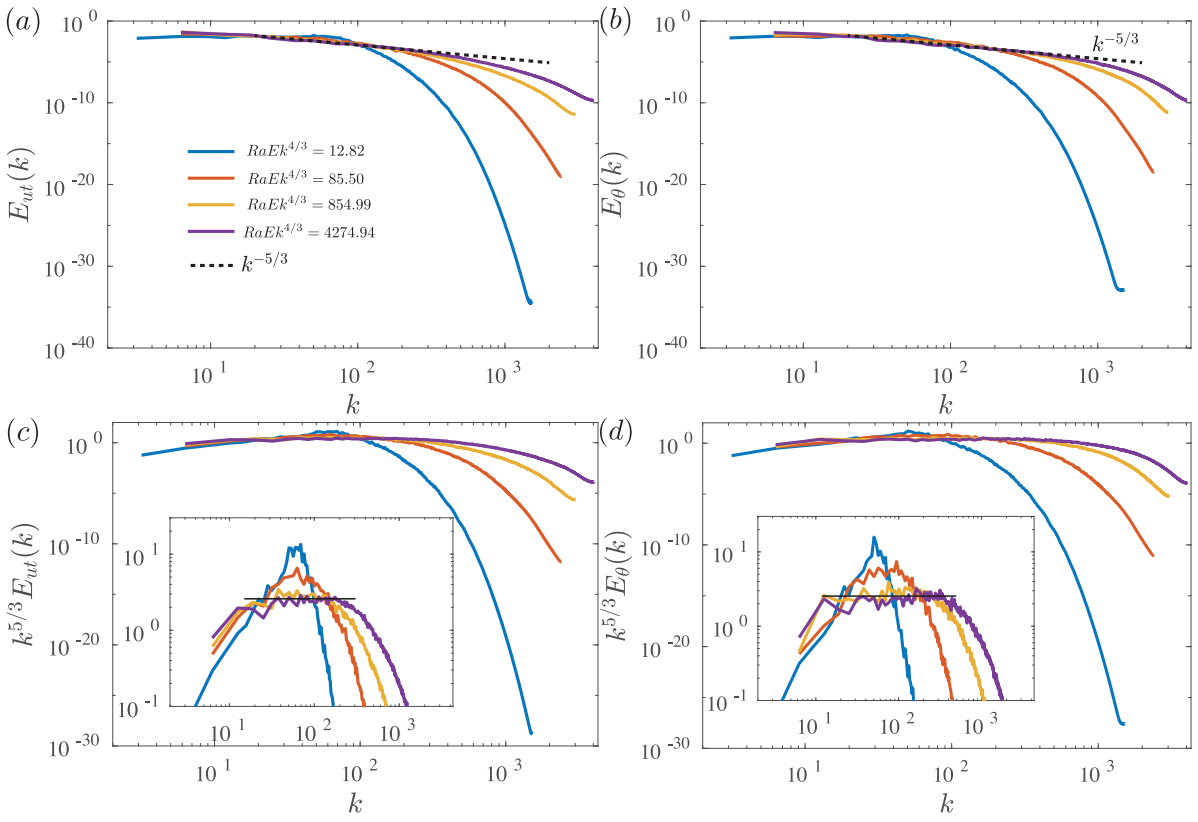

Fig. 8. (*a*) Turbulent kinetic energy spectra $E_{ut}(k)$ normalized by $u_t^2/2$ and (*b*) temperature energy spectra $E_\theta(k)$ normalized by $\theta^2/2$, sampled at the mid height of the domain. The spectra are plotted as functions of normalized wavenumber k for the cells, plumes, rotation-affected, and buoyancy-dominated turbulent regimes, at $Ek = 5\times10^{-6}$ and different Ra. The compensated forms for (*c*) the turbulent kinetic energy spectra $k^{5/3}E_{ut}(k)$ and (*d*) temperature energy spectra $k^{5/3}E_\theta(k)$. The inset shows the zoom in plot where the scaling exponent of $-5/3$ is achieved.

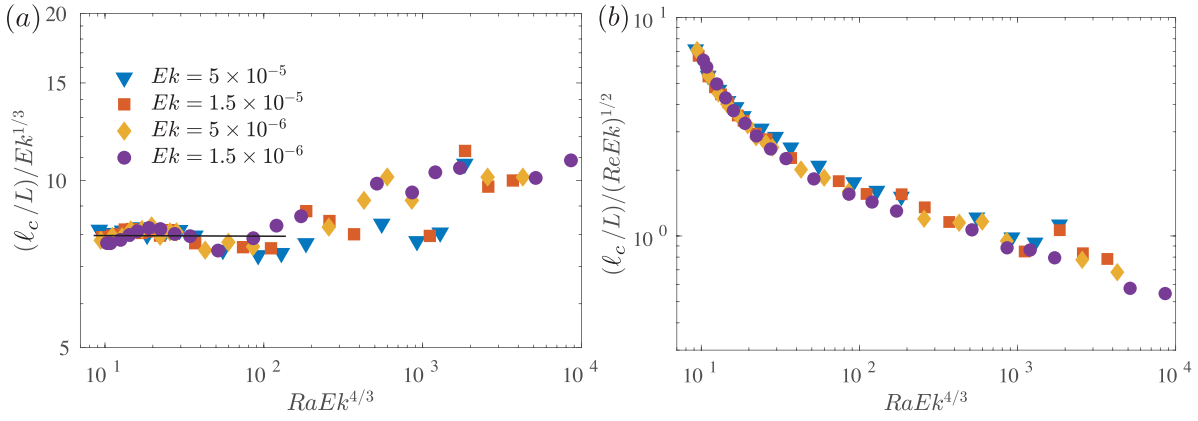

Fig. 9. Dimensionless convective length scale ℓ_c/L, as obtained in the DNS, and compensated with the (*a*) the onset length scale of $\sim Ek^{1/3}$ and (*b*) the inertia length scale of $\sim (ReEk)^{1/2}$, as functions of $RaEk^{4/3}$.

dimensional energy spectra are calculated based on the fluctuations of three velocity components and temperature at the middle height plane. When we calculate the Fourier transform in the $x-$ ($y-$) direction, it is averaged in the $y-$ ($x-$) direction (i.e. in another horizontal direction). The energy spectra in two horizontal directions show very similar results. All values of k are integer multiples of $2\pi/d$ and they are normalized by the domain height L. As presented in Fig. 8(*a, b*), the values of $E_{ut}(k)$ and $E_\theta(k)$ show very similar energy distributions in the spatial wave number space for each of the four different flow regimes. The distinct peak in the low wavenumber range for the cell regime disappears with increasing Ra and the energy in the high wavenumber range increases monotonically, which confirms that more small-scale flow fluctuations are excited in the rotation-affected and buoyancy-dominated turbulent regimes. Moreover, the increase of Ra leads to a gradual development of a scaling range close to $-5/3$, which is the hallmark of classical three-dimensional inertial turbulence (see also Fig. 8*c, d*).

To quantify the global heat and momentum transport as well as the characteristic convective length scale scaling relations during the whole transition pathway, we first recall the two important force balances that determine various heat and momentum transfer scaling relations in RRBC. On the one hand, the balance of the viscous, buoyancy, and Coriolis forces, i.e. the so-called VAC balance, gives to the onset length scale of $\ell/L \sim Ek^{1/3}$ and the following momentum transfer

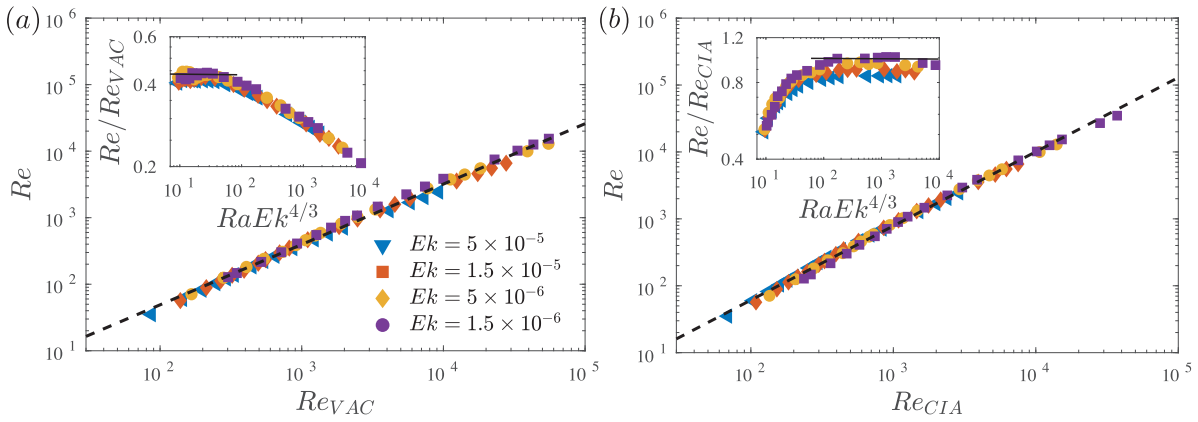

Fig. 10. (*a*) Re versus Re_{VAC}, where the best fit dashed line is given as $Re = (0.75 \pm 0.07) Re_{VAC}^{0.91 \pm 0.01}$; (*b*) Re versus Re_{CIA}, where the best fit dashed line is $Re = (0.37 \pm 0.03) Re_{CIA}^{1.11 \pm 0.01}$. The insets show the compensated plots of Re/Re_{VAC} and Re/Re_{CIA} versus $RaEk^{4/3}$. The symbols have the same meaning as in Fig. 2.

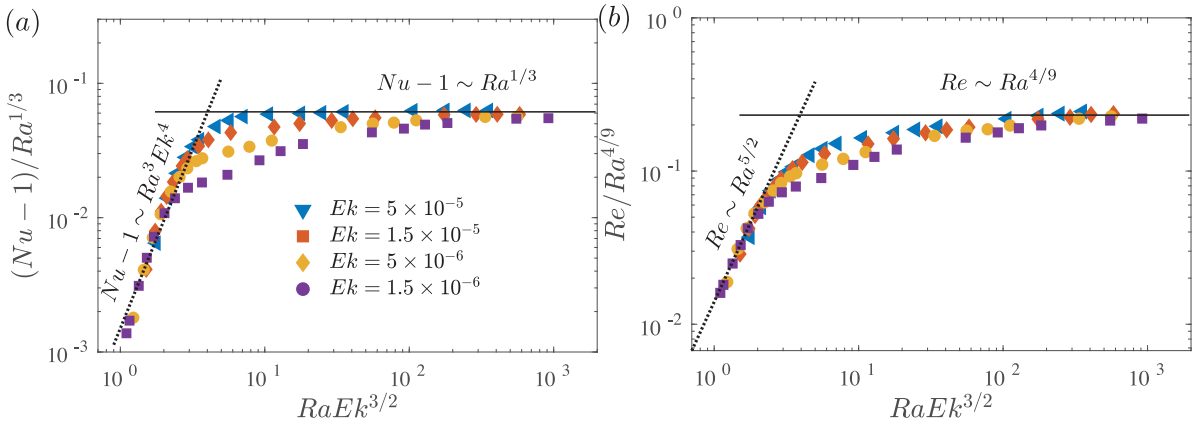

Fig. 11. (*a*) Representation of Nu displaying the transition from the rotation-dominated regime ($Nu - 1 \sim (RaEk^{4/3})^{\xi}$) to the buoyancy-dominated regime ($Nu - 1 \sim Ra^{\gamma}$). The black dotted line denotes the steep scaling of $Nu - 1 \sim Ra^3 Ek^4$ in the rotation-dominated regime and the solid line corresponds to the classical regime of non-rotating scaling of $Nu - 1 \sim Ra^{1/3}$, respectively. (*b*) The corresponding representation of Re scaling displays the transition. The black dotted line denotes the scaling of $Re \sim Ra^{5/2}$ in the rotation-dominated regime and the solid line corresponds to the classical regime of non-rotating scaling of $Re \sim Ra^{4/9}$, respectively. The symbols have the same meaning as in Fig. 2.

scaling [13,59,60]:

$$Re_{VAC} \sim Ra^{1/2}(Nu-1)^{1/2} Pr^{-1} Ek^{1/3}. \tag{4}$$

On the other hand, the balance of the Coriolis and inertial forces leads to $\ell/L \sim (u/2\Omega L)^{1/2} = Ro_c^{1/2} = (ReEk)^{1/2}$, proposed for the case when the viscosity effects are negligible in a fully developed turbulent state. The balance of CIA forces gives rise to

$$Re_{CIA} \sim Ra^{2/5}(Nu-1)^{2/5} Pr^{-4/5} Ek^{1/5}. \tag{5}$$

We first check the scaling relation of the convective length scale. Based on the energy spectra, we can calculate the characteristic convective length scale during the flow transition pathway. Specifically, we calculate the dimensionless bulk convective length scale ℓ_c/L based on the vertical velocity as

$$\ell_c/L = \sum_k [\hat{u}_z(k)\hat{u}_z^*(k)] / \sum_k k[\hat{u}_z(k)\hat{u}_z^*(k)]. \tag{6}$$

Here, $\hat{u}_i(k)$ and $\hat{u}_i^*(k)$ are, respectively, the Fourier transforms of u_i and its complex conjugate at the middle height and k is the wavenumber. We calculate the above equation in two horizontal directions (x and y) and then get the averaged value for the convective length scale. As demonstrated in Fig. 9(*a*), the convective length scale is shown to follow the onset length scale of $Ek^{1/3}$ quite well for the rotation-dominated regime, where $RaEk^{4/3} \leq 200$. After $RaEk^{4/3} > 200$ at rotation-affected and buoyancy-dominated regime, the length scale gradually deviates from this onset length scale. For a constant Ek, as Ra gets higher, the flow state undergoes a transition from the rotation-dominated regime to the buoyancy-dominated regime. In the rotation-dominated cell and columnar regimes, the onset length scale as $\ell/L \sim Ek^{1/3}$ [7,23], while in the buoyancy-dominated regime, the dominant length will be the domain height L as the flow is controlled by the large-scale circulations that span across the bottom and top walls [3]. Hence, the increasing Ra gradually changes the convective length scale from $\ell/L \sim Ek^{1/3}$ to $\ell/L \sim 1$. However, the length scale compensated with the inertial length scale of $(ReEk)^{1/2}$ in Fig. 9(*b*) does not show a flat range for the whole transition pathway. This means that the inertial length scale $(ReEk)^{1/2}$ does not hold for all these flow states, which was also expected, since the CIA force-balance is only valid in the geostrophic turbulence regime [13,39,58,80].

Furthermore, we check the above Re_{VAC} and Re_{CIA} scaling relations for various flow regimes. Here, the vertical velocity is used to define the Reynolds number ($Re = \sqrt{\langle u_z \rangle^2} L/\nu$) [60,85]. As demonstrated in Fig. 10(*a*, *b*), both scaling relations show a very good collapse within the whole parameter range. The best fit of the VAC scaling is $Re = (0.75 \pm 0.07) Re_{VAC}^{0.91 \pm 0.001}$ and the best fit of the CIA scaling is $Re = (0.37 \pm 0.03) Re_{CIA}^{1.11 \pm 0.01}$ with 95% confidence. To determine which force balance induced Re scaling relation matches the different flow states better, we present compensated plots for these two Re scaling relations in the insets. In Fig. 10(*a*) inset, after a short flat range of $RaEk^{4/3} \lesssim 40$, the compensated value decreases monotonically, which implies that the VAC-based Re-scaling agrees well only with the data in the cellular and columnar regimes. While in Fig. 10(*b*) inset, the

compensated value increases monotonically until $RaEk^{4/3} \approx 200$ and then reaches a plateau, indicating that the CIA-based Re-scaling agrees well with the data in the rotation-affected and buoyancy-dominated turbulent regimes. Moreover, the valid range of CIA-based Re-scaling has a prefactor close to 1, which is believed to be achieved only in the geostrophic turbulence regime [60]. However, according to our recent study [38], whether the geostrophic turbulence regime is achieved or not, should be judged based on the three diffusion-free scaling relations for the convective heat transport $Nu-1$, momentum transport Re and convective length scale ℓ_c/L. Our scaling argument in [38] suggests that all three scaling relations (for $Nu-1, Re, \ell_c/L$) should hold simultaneously to characterize the system as a geostrophic turbulence regime.

To build a connection between rapidly rotating convection and weakly rotating convection, a common and practical way is to analyse the typical heat transport scaling relations measured in different regimes of the convection system. To quantitatively describe the heat transport transition from the rotation-dominated ($Nu \sim (RaEk^{4/3})^{\xi}$) regime to the buoyancy-dominated ($Nu \sim Ra^{\gamma}$) regime, in [6], a unifying scaling approach was proposed, where the change in the Ekman and thermal BL thicknesses balance [15] was also taken into account. In this approach [6], the balance of the thicknesses of the viscous Ekman BL, $\delta_u/L \sim Ek^{1/2}$ and the thermal BL, $\delta_\theta/L \sim Nu^{-1}$ was considered. When the flow undergoes the transition from the rotation-dominated regime to the buoyancy-dominated regime, the different heat transport scaling relations that hold in these regimes will give similar results:

$$Nu \sim (RaEk^{4/3})^{\xi} \sim Ra^{\gamma}. \tag{7}$$

Moreover, the two BL thicknesses should scale similarly [6], therefore

$$Nu^{-1} \sim \delta_\theta/L \sim \delta_u/L \sim Ek^{1/2}. \tag{8}$$

It was derived in [6] that the exponents ξ and γ are related as $\gamma = 3\xi/(3+8\xi)$. For the buoyancy-dominated turbulent regime, the exponent γ is readily available through the Grossmann–Lohse theory [53,74,86]. The transition theory about the heat transfer scaling agrees well with Nu results obtained from experiments and DNS with no-slip boundary conditions [6]. Here, we also use this transition theory to examine the present DNS data. Specifically, the model suggests that for the non-rotating convection regime, the classical scaling regime of $\sim Ra^{1/3}$ ($\gamma = 1/3$) will lead to the steep heat transfer scaling of $\sim Ra^3 Ek^4$ ($\xi = 3$) for the rotation-dominated regime. As demonstrated in Fig. 11(a), these two asymptotic heat transfer scaling relations are well realized in the range of $1 \lesssim RaEk^{3/2} \lesssim 4$ and $RaEk^{3/2} \gtrsim 300$ for the present DNS results. With higher Ek, these heat transfer scaling relations fit the data with a broader range. (Note that recently, the unifying model for the transition in RRBC [6] was extended also to magnetoconvection [87].)

Correspondingly, the global momentum transport scaling relation for the classical regime of non-rotating convection is $Re \sim Ra^{4/9}$ [53]. In the rotation-dominated regime, a relation of $Re \sim Ra^{5/2}$ has been obtained from our recent theoretical derivation [38]. To this end, as shown in Fig. 11(b), the Re data plotted with the same parameter $RaEk^{3/2}$ are also bounded by $Re \sim Ra^{5/2}$ in the rotation-dominated regime and $Re \sim Ra^{4/9}$ in the buoyancy-dominated regime. Hence, this transition theory that described the heat transport scaling from rapidly rotating convection to weakly rotating convection is supported by present DNS data. We further verify that the corresponding momentum transport scaling can also be interpreted similarly: it changes smoothly from the rotation-dominated Re-scaling to the non-rotating convection Re-scaling relation.

As we mentioned in the introduction section, only a few studies have explored how to quantify the connection between the two distinct regimes and the transition process from rotation-dominated to buoyancy-dominated convection, see e.g., [6,13,15,32,51]. Via the different balances between the Coriolis, inertial, Archimedean and viscous forces, Aurnou et al. [13] derived a series of heat and momentum transport and convective length scale scaling relations for the asymptotic non-rotating and rapidly rotating states with both, applied

Table A.1
Summary of the quantities in the present DNS of RRBC (the non-rotating cases are not shown here, we refer to [63]). All simulations are performed at $Pr = 1$. Here, Ra is the Rayleigh number, Ro_c the convective Rossby number, Re the Reynolds number, Ek the Ekman number, $\Gamma = d/L$ the aspect ratio, where d is the width of the plate and L the domain height. The averaged Nusselt number Nu is calculated from the Nu-values evaluated in five different ways: at the bottom and top plates, by volume-averaging, from the kinetic energy and thermal dissipation rates. The 'Error' denotes the maximum relative error between each two of these values. The last column represents the grid mesh sizes used in the vertical (N_z) and two horizontal (N_x, N_y) directions.

No.	Ra	Ro_c	Re	Nu	Error	$N_z \times N_x \times N_y$
			$Ek = 5.0\times10^{-5}$, $\Gamma = 4.0$			
1	5.0×10^6	0.112	35.17	2.11	0.09%	$108\times864\times864$
2	6.0×10^6	0.123	59.72	3.54	0.22%	$108\times864\times864$
3	7.0×10^6	0.132	82.05	5.09	0.29%	$108\times864\times864$
4	8.0×10^6	0.141	102.87	6.63	0.37%	$108\times864\times864$
5	9.0×10^6	0.150	121.47	8.04	0.36%	$109\times864\times864$
6	1.0×10^7	0.158	137.76	9.20	0.60%	$144\times1152\times1152$
7	1.3×10^7	0.180	184.13	12.21	0.41%	$144\times1152\times1152$
8	1.6×10^7	0.200	222.44	14.35	0.41%	$144\times1152\times1152$
9	2.0×10^7	0.224	265.49	16.36	0.41%	$144\times1152\times1152$
10	3.0×10^7	0.274	346.20	19.33	0.24%	$192\times1536\times1536$
11	5.0×10^7	0.354	469.78	23.02	0.33%	$192\times1536\times1536$
			$\Gamma = 1.0$			
12	7.0×10^7	0.418	572.72	25.88	0.38%	$256\times384\times384$
13	1.0×10^8	0.500	704.23	29.47	0.28%	$256\times384\times384$
14	3.0×10^8	0.866	1283.29	42.86	0.44%	$256\times384\times384$
15	5.0×10^8	1.118	1689.76	50.92	0.71%	$256\times384\times384$
16	7.0×10^8	1.323	2024.55	56.77	1.09%	$256\times384\times384$
17	1.0×10^9	1.581	2446.13	63.84	0.48%	$256\times384\times384$
			$Ek = 1.5\times10^{-5}$, $\Gamma = 2.0$			
17	2.6×10^7	0.076	56.74	2.22	0.27%	$144\times576\times576$
18	3.0×10^7	0.082	88.80	3.46	0.17%	$144\times576\times576$
19	3.3×10^7	0.086	112.77	4.57	0.30%	$144\times576\times576$
20	3.6×10^7	0.090	136.28	5.75	0.23%	$144\times576\times576$
21	4.0×10^7	0.095	162.20	7.31	0.24%	$192\times768\times768$
22	4.6×10^7	0.102	206.85	9.71	0.36%	$192\times768\times768$
23	5.0×10^7	0.106	234.42	11.13	0.40%	$192\times768\times768$
24	6.0×10^7	0.116	296.50	14.34	0.69%	$192\times768\times768$
25	7.0×10^7	0.126	349.33	16.64	0.46%	$192\times768\times768$
26	1.0×10^8	0.150	466.20	20.97	0.20%	$256\times1024\times1024$
27	2.0×10^8	0.212	734.67	28.68	0.28%	$256\times1024\times1024$
28	3.0×10^8	0.260	952.62	34.59	0.35%	$256\times1024\times1024$
			$\Gamma = 1.0$			
29	5.0×10^8	0.335	1305.93	42.98	0.31%	$384\times512\times512$
30	7.0×10^8	0.397	1585.48	49.39	0.23%	$384\times512\times512$
31	1.0×10^9	0.474	1934.75	56.40	0.38%	$512\times960\times960$
32	3.0×10^9	0.822	3556.12	85.16	0.52%	$512\times960\times960$
33	5.0×10^9	1.061	4591.39	101.31	0.32%	$512\times960\times960$
34	7.0×10^9	1.255	5556.48	113.50	0.55%	$512\times960\times960$
35	1.0×10^{10}	1.500	6591.31	127.39	0.56%	$640\times1200\times1200$
			$Ek = 5.0\times10^{-6}$, $\Gamma = 2.0$			
35	1.1×10^8	0.052	70.75	1.86	0.15%	$240\times960\times960$
36	1.3×10^8	0.057	125.14	3.07	0.23%	$240\times960\times960$
37	1.5×10^8	0.061	181.60	4.78	0.29%	$240\times960\times960$
38	1.7×10^8	0.065	240.21	6.88	0.25%	$240\times960\times960$
39	2.0×10^8	0.071	306.57	10.14	0.19%	$256\times1024\times1024$
40	2.3×10^8	0.076	387.91	13.31	0.70%	$256\times1024\times1024$
41	2.6×10^8	0.081	458.92	15.88	0.35%	$256\times1024\times1024$
42	3.0×10^8	0.087	540.43	18.63	0.30%	$256\times1024\times1024$
43	3.3×10^8	0.091	590.79	20.13	0.27%	$256\times1024\times1024$
44	5.0×10^8	0.112	809.44	25.63	0.28%	$288\times1152\times1152$
45	7.0×10^8	0.132	1025.23	30.94	0.37%	$288\times1152\times1152$
			$\Gamma = 1.0$			
46	1.0×10^9	0.158	1329.35	38.46	0.27%	$384\times768\times768$
47	3.0×10^9	0.274	2765.88	69.03	0.50%	$384\times768\times768$
48	5.0×10^9	0.354	3757.87	86.80	0.76%	$384\times768\times768$
49	7.0×10^9	0.418	4450.86	98.53	0.51%	$512\times960\times960$
50	1.0×10^{10}	0.500	5521.25	115.18	0.51%	$512\times960\times960$
51	3.0×10^{10}	0.866	9959.97	174.84	0.51%	$512\times960\times960$
52	5.0×10^{10}	1.118	12 939.48	208.96	0.44%	$640\times1280\times1280$

(*continued on next page*)

Table A.1 (*continued*).

No.	*Ra*	Ro_c	*Re*	*Nu*	Error	$N_z \times N_x \times N_y$
			$Ek = 1.5 \times 10^{-6}$, $\Gamma = 1.0$			
53	6.0×10^8	0.037	127.68	2.16	0.10%	$288 \times 576 \times 576$
54	6.3×10^8	0.038	147.28	2.48	0.14%	$288 \times 576 \times 576$
55	7.3×10^8	0.041	206.14	3.79	0.31%	$288 \times 576 \times 576$
56	8.3×10^8	0.043	302.36	5.73	0.21%	$288 \times 576 \times 576$
57	9.3×10^8	0.046	393.01	8.06	0.14%	$384 \times 768 \times 768$
58	1.1×10^9	0.050	548.44	12.16	0.40%	$384 \times 768 \times 768$
59	1.3×10^9	0.054	708.88	16.24	0.86%	$384 \times 768 \times 768$
60	1.6×10^9	0.060	895.37	20.54	0.54%	$384 \times 768 \times 768$
61	2.0×10^9	0.067	1078.28	24.03	0.31%	$384 \times 768 \times 768$
62	3.0×10^9	0.082	1466.82	30.94	0.33%	$384 \times 768 \times 768$
63	5.0×10^9	0.106	2242.54	46.71	0.28%	$432 \times 864 \times 864$
64	7.0×10^9	0.126	2938.62	60.83	0.30%	$512 \times 1024 \times 1024$
65	1.0×10^{10}	0.150	3839.60	77.58	0.55%	$512 \times 1024 \times 1024$
66	3.0×10^{10}	0.260	7488.58	135.00	0.70%	$512 \times 1024 \times 1024$
67	5.0×10^{10}	0.335	10 167.53	170.47	0.60%	$512 \times 1024 \times 1024$
			$\Gamma = 0.5$			
68	7.0×10^{10}	0.397	12 582.42	204.13	0.51%	$1024 \times 512 \times 512$
69	1.0×10^{11}	0.474	15 373.78	236.11	0.82%	$1536 \times 768 \times 768$
70	3.0×10^{11}	0.822	26 945.29	365.96	0.73%	$1536 \times 768 \times 768$
71	5.0×10^{11}	1.061	34 828.68	437.60	0.99%	$1920 \times 960 \times 960$

temperature drop across the domain and applied heat flux conditions. Other studies are based on the BL control hypothesis proposed in [15]. Specifically, the use of an empirical scaling for non-rotating heat transfer $Nu \sim Ra^{2/7}$ [15] gives a transition parameter of $RaEk^{7/4}$. Similarly, according to the framework of a marginally stable thermal boundary layer, a transition parameter of $RaEk^{3/2}$ has been obtained in [32]. Specifically, the relation $RaEk^{3/2} = \mathcal{O}(1)$ has been demonstrated to properly describe the transition between the geostrophic and weakly rotating convection regimes, regarding the thermal and velocity BL thicknesses, interior temperature gradients, heat transport and flow speed behaviours (Péclet numbers) [32,51,88]. Based on the balance of the thermal and viscous (Ekman) BL thicknesses, the unifying transition scaling model proposed in [6] mainly connects the heat transport scaling relations in the rotation-dominated and buoyancy-dominated regimes. For example, the classical scaling of $Nu \sim Ra^{1/3}$ in the non-rotating convection leads to a steep heat transport of $Nu \sim Ra^3Ek^4$ in the rotation-dominated regime. Consistent with [32], this model also leads to the transition parameter scale $RaEk^{3/2}$. Moreover, based on the *Re* scaling relations found in the non-rotating and rapidly rotating convection, we can also quantify the smooth transition of momentum transport scaling with this transition parameter $RaEk^{3/2}$.

4. Conclusions

A comprehensive transition pathway from rotation-dominated to buoyancy-dominated flows in RRBC has been realized and investigated thoroughly via DNS. The DNS are performed in the planar geometry in laterally periodic domains with realistic no-slip top and bottom boundary conditions. The detailed hydrodynamic fields obtained in the DNS have enabled us to quantify the full transition dynamics and flow structures among different flow regimes. Specifically, the vertically aligned flow structures in the rotation-dominated regime gradually lose coherence with the enhanced thermal driving force and eventually form large-scale circulations in the buoyancy-dominated turbulent regime. The corresponding change of the mean temperature profile and its gradient at the middle height is demonstrated to be very useful qualitative characteristic for the distinct flow regimes during the whole transition pathway, especially for the cellular, columnar, and plume regimes of rotation-dominated convection. According to our DNS data, the crossover between the thermal and Ekman BL thicknesses is well captured by the transition parameter $RaEk^{7/4} \approx 1$ proposed in [15]. However, $RaEk^{7/4}$ is just an approximation of $RaEk^{3/2}$, which is proposed to quantify the scaling of the transition between rotation-dominated and buoyancy-dominated regimes, for the considered range of *Ra* and *Ek*.

One of the most interesting aspects of RRBC is the different scaling behaviours of the global heat and momentum transport as well as the characteristic convective length scale in different flow regimes. In the rotation-dominated regime, a steep heat transport is obtained and the convective length scale is shown to follow the onset length scale of $\ell/L \sim Ek^{1/3}$. Meanwhile, the global momentum transport agrees with the VAC-*Re* scaling quite well in the cellular and columnar regimes. However, in the rotation-affected and buoyancy-dominated turbulence regimes, the heat transport behaves close to that in the non-rotating case, while neither the onset scale nor the inertial length scale $(ReEk)^{1/2}$ are valid. However, the CIA-*Re* scaling is achieved for the momentum transport, which is believed to hold in the geostrophic turbulence regime. This suggests that the convective length scale is highly relevant in the transition dynamics in RRBC. This also inspires consideration of other parameters that can quantify the scaling of the transition between different flow regimes.

To this end, the global heat and momentum transport scaling behaviours during this transition were studied. It was demonstrated that they are well captured by the unified transition scaling model [6]. An interesting result of our study is that the derived scaling of the transition between the two regimes is seen not only in the heat transport but also in the momentum transport, see Fig. 11 (*a, b*). All heat and momentum transport scaling relations obtained from our DNS data vary between the limiting theoretical scaling relations for the rotation-dominated and buoyancy-dominated regimes.

CRediT authorship contribution statement

Jiaxing Song: Writing – review & editing, Writing – original draft, Visualization, Validation, Software, Resources, Methodology, Investigation, Funding acquisition, Formal analysis, Conceptualization. **Veeraraghavan Kannan:** Writing – review & editing, Writing – original draft, Validation, Software, Methodology. **Olga Shishkina:** Writing – review & editing, Writing – original draft, Validation, Supervision, Conceptualization. **Xiaojue Zhu:** Writing – review & editing, Writing – original draft, Supervision, Resources, Project administration, Funding acquisition, Formal analysis, Conceptualization.

Declaration of competing interest

The authors declare that they have no known competing financial interests or personal relationships that could have appeared to influence the work reported in this paper.

Data availability

Data will be made available on request.

Acknowledgements

The authors acknowledge the financial support from the Alexander von Humboldt Foundation Fellowship, Germany, the Max Planck Society, Germany, and the German Research Foundation (DFG), Sh405/20, Sh405/22, 521319293, 540422505 and 550262949. The authors gratefully acknowledge the computing time provided to them on the high-performance computer Lichtenberg at the NHR Centers NHR4CES at TU Darmstadt, funded by the Federal Ministry of Education and Research, Germany, and the state governments participating on the basis of the resolutions of the GWK for national high-performance computing at universities, on the HPC systems of Max Planck Computing and Data Facility (MPCDF), on the HoreKa supercomputer funded by the Ministry of Science, Research and the Arts Baden-Württemberg and by the Federal Ministry of Education and Research, and on the GCS Supercomputer SuperMUC-NG at Leibniz Supercomputing Centre (LRZ).

Appendix. Numerical parameters and grid resolutions

See Table A.1.

References

[1] F.H. Busse, C.R. Carrigan, Laboratory simulation of thermal convection in rotating planets and stars, Science 191 (1976) 81–83.
[2] J.J. Niemela, L. Skrbek, K.R. Sreenivasan, R.J. Donnelly, Turbulent convection at very high Rayleigh numbers, Nature 404 (2000) 837–840.
[3] G. Ahlers, S. Grossmann, D. Lohse, Heat transfer and large scale dynamics in turbulent Rayleigh–Bénard convection, Rev. Modern Phys. 81 (2009) 503.
[4] J.M. Aurnou, M.A. Calkins, J.S. Cheng, K. Julien, E. King, D. Nieves, K.M. Soderlund, S. Stellmach, Rotating convective turbulence in Earth and planetary cores, Phys. Earth Planet. Inter. 246 (2015) 52–71.
[5] C. Guervilly, P. Cardin, N. Schaeffer, Turbulent convective length scale in planetary cores, Nature 570 (2019) 368–371.
[6] R.E. Ecke, O. Shishkina, Turbulent rotating Rayleigh–Bénard convection, Annu. Rev. Fluid Mech. 55 (2023) 603–638.
[7] S. Chandrasekhar, The instability of a layer of fluid heated below and subject to Coriolis forces, Proc. R. Soc. Lond. A 217 (1953) 306–327.
[8] H.T. Rossby, A study of Bénard convection with and without rotation, J. Fluid Mech. 36 (1969) 309–335.
[9] K.L. Chong, Y. Yang, S. Huang, J. Zhong, R.J.A.M. Stevens, R. Verzicco, D. Lohse, K. Xia, Confined Rayleigh–Bénard, rotating Rayleigh–Bénard, and double diffusive convection: A unifying view on turbulent transport enhancement through coherent structure manipulation, Phys. Rev. Lett. 119 (2017) 064501.
[10] R.P.J. Kunnen, The geostrophic regime of rapidly rotating turbulent convection, J. Turbul. 22 (2021) 267–296.
[11] D. Lohse, K.-Q. Xia, Small-scale properties of turbulent Rayleigh–Bénard convection, Annu. Rev. Fluid Mech. 42 (2010) 335–364.
[12] O. Shishkina, Rayleigh–Bénard convection: The container shape matters, Phys. Rev. Fluids 6 (2021) 090502.
[13] J.M. Aurnou, S. Horn, K. Julien, Connections between nonrotating, slowly rotating, and rapidly rotating turbulent convection transport scalings, Phys. Rev. Res. 2 (2020) 043115.
[14] A.J. Aguirre Guzmán, M. Madonia, J.S. Cheng, R. Ostilla-Mónico, H.J.H. Clercx, R.P.J. Kunnen, Force balance in rapidly rotating Rayleigh–Bénard convection, J. Fluid Mech. 928 (2021) A16.
[15] E.M. King, S. Stellmach, J. N., U. Hansen, J.M. Aurnou, Boundary layer control of rotating convection systems, Nature 457 (2009) 301–304.
[16] M. Plumley, K. Julien, Scaling laws in Rayleigh–Bénard convection, Earth Space Sci. 34 (2019) 1580–1592.
[17] H.P. Greenspan, The Theory of Rotating Fluids, Cambridge University Press, 1968.
[18] G.I. Taylor, Experiments with rotating fluids, Proc. R. Soc. Lond. Ser. A Math. Phys. Eng. Sci. 100 (1921) 114–121.
[19] J. Proudman, On the motion of solids in a liquid possessing vorticity, Proc. R. Soc. Lond. Ser. A Math. Phys. Eng. Sci. 92 (1916) 408–424.
[20] K. Julien, A.M. Rubio, I. Grooms, E. Knobloch, Statistical and physical balances in low Rossby number Rayleigh–Bénard convection, Geophys. Astrophys. Fluid Dyn. 106 (2012) 392–428.
[21] S. Stellmach, M. Lischper, K. Julien, G. Vasil, J.S. Cheng, A. Ribeiro, E.M. King, J.M. Aurnou, Approaching the asymptotic regime of rapidly rotating convection: Boundary layers versus interior dynamics, Phys. Rev. Lett. 113 (2014) 254501.
[22] A.J.A. Aguirre Guzmán, M. Madonia, J.S. Cheng, R. Ostilla-Mónico, H.J.H. Clercx, R.P.J. Kunnen, Competition between Ekman plumes and vortex condensates in rapidly rotating thermal convection, Phys. Rev. Lett. 125 (2020) 214501.
[23] S. Chandrasekhar, Hydrodynamic and Hydromagnetic Stability, Oxford University Press, 1961.
[24] R. Ecke, F. Zhong, E. Knobloch, Hopf bifurcation with broken reflection symmetry in rotating Rayleigh–Bénard convection, Europhys. Lett. 19 (3) (1992) 177–182.
[25] F. Zhong, R.E. Ecke, V. Steinberg, Rotating Rayleigh–Bénard convection: asymmetric modes and vortex states, J. Fluid Mech. 249 (1993) 135–159.
[26] H.F. Goldstein, E. Knobloch, I. Mercader, M. Net, Convection in a rotating cylinder. Part 1 Linear theory for moderate Prandtl numbers, 248, 1993, pp. 583–604.
[27] B. Favier, E. Knobloch, Robust wall states in rapidly rotating Rayleigh–Bénard convection, J. Fluid Mech. 895 (2020) R1.
[28] O. Shishkina, Tenacious wall states in thermal convection in rapidly rotating containers, J. Fluid Mech. 898 (2020) F1.
[29] X. Zhang, D.P.M. van Gils, S. Horn, M. Wedi, L. Zwirner, G. Ahlers, R.E. Ecke, S. Weiss, E. Bodenschatz, O. Shishkina, Boundary zonal flows in rotating turbulent Rayleigh–Bénard convection, Phys. Rev. Lett. 124 (2020) 084505.
[30] X. Zhang, R.E. Ecke, O. Shishkina, Boundary zonal flows in rapidly rotating turbulent thermal convection, J. Fluid Mech. 915 (2021) A62.
[31] X.M. de Wit, A.J.A. Guzmán, M. Madonia, J.S. Cheng, H.J.H. Clercx, R.P.J. Kunnen, Turbulent rotating convection confined in a slender cylinder: The sidewall circulation, Phys. Rev. Fluids 5 (1) (2020) 023502.
[32] E.M. King, S. Stellmach, J.M. Aurnou, Heat transfer by rapidly rotating Rayleigh–Bénard convection, J. Fluid Mech. 691 (2012) 568–582.
[33] K. Julien, J.M. Aurnou, M.A. Calkins, E. Knobloch, P. Marti, S. Stellmach, G.M. Vasil, A nonlinear model for rotationally constrained convection with Ekman pumping, J. Fluid Mech. 798 (2016) 50–87.
[34] M. Plumley, K. Julien, P. Marti, S. Stellmach, The effects of Ekman pumping on quasi-geostrophic Rayleigh–Bénard convection, J. Fluid Mech. 803 (2016) 51–71.
[35] B.M. Boubnov, G.S. Golitsyn, Temperature and velocity field regimes of convective motions in a rotating plane fluid layer, J. Fluid Mech. 219 (1990) 215–239.
[36] S. Horn, O. Shishkina, Rotating non-Oberbeck–Boussinesq Rayleigh–Bénard convection in water, Phys. Fluids 26 (2014) 055111.
[37] S. Horn, O. Shishkina, Toroidal and poloidal energy in rotating Rayleigh–Bénard convection, J. Fluid Mech. 762 (2015) 232–255.
[38] J. Song, O. Shishkina, X. Zhu, Scaling regimes in rapidly rotating thermal convection at extreme Rayleigh numbers, J. Fluid Mech. 984 (2024) A45.
[39] J. Song, O. Shishkina, X. Zhu, Direct numerical simulations of rapidly rotating Rayleigh–Bénard convection with Rayleigh number up to 5×10^{13}, J. Fluid Mech. (2024) in print.
[40] R.E. Ecke, J.J. Niemela, Heat transport in the geostrophic regime of rotating Rayleigh–Bénard convection, Phys. Rev. Lett. 113 (2014) 114301.
[41] A.M. Rubio, K. Julien, E. Knobloch, J.B. Weiss, Upscale energy transfer in three-dimensional rapidly rotating turbulent convection, Phys. Rev. Lett. 112 (2014) 144501.
[42] C. Guervilly, D.W. Hughes, Jets and large-scale vortices in rotating Rayleigh–Bénard convection, Phys. Rev. Fluids 2 (1) (2017) 113503.
[43] S. Weiss, G. Ahlers, Heat transport by turbulent rotating Rayleigh–Bénard convection and its dependence on the aspect ratio, J. Fluid Mech. 684 (2011) 1–20.
[44] S. Weiss, G. Ahlers, The large-scale flow structure in turbulent rotating Rayleigh–Bénard convection, J. Fluid Mech. 688 (2011) 461–492.
[45] J.S. Cheng, J.M. Aurnou, K. Julien, R.P.J. Kunnen, A heuristic framework for next-generation models of geostrophic convective turbulence, Geophys. Astrophys. Fluid Dyn. 112 (2018) 277–300.
[46] J.S. Cheng, M. Madonia, A.J.A. Guzmán, R.P.J. Kunnen, Laboratory exploration of heat transfer regimes in rapidly rotating turbulent convection, Phys. Rev. Fluids 5 (11) (2020) 113501.
[47] M. Wedi, V.M. Moturi, D. Funfschilling, S. Weiss, Experimental evidence for the boundary zonal flow in rotating Rayleigh–Bénard convection, J. Fluid Mech. 939 (2022) A14.
[48] R.J.A.M. Stevens, H.J.H. Clercx, D. Lohse, Optimal Prandtl number for heat transfer in rotating Rayleigh–Bénard convection, New J. Phys. 12 (2010) 075005.
[49] Y. Yang, R. Verzicco, D. Lohse, R.J.A.M. Stevens, What rotation rate maximizes heat transport in rotating Rayleigh–Bénard convection with Prandtl number larger than one? Phys. Rev. Fluids 5 (2020) 053501.
[50] Y. Liu, R.E. Ecke, Heat transport measurements in turbulent rotating Rayleigh–Bénard convection, Phys. Rev. E 80 (2009) 036314.
[51] E.M. King, S. Stellmach, B. Buffett, Scaling behaviour in Rayleigh–Bénard convection with and without rotation, J. Fluid Mech. 717 (2013) 449–471.
[52] H. Lu, G. Ding, J. Shi, K. Xia, J. Zhong, Heat-transport scaling and transition in geostrophic rotating convection with varying aspect ratio, Phys. Rev. Fluids 6 (2021) L071501.
[53] S. Grossmann, D. Lohse, Scaling in thermal convection: a unifying theory, J. Fluid Mech. 407 (2000) 27–56.
[54] S. Grossmann, D. Lohse, Multiple scaling in the ultimate regime of thermal convection, Phys. Fluids 23 (2011) 045108.
[55] M. Sprague, K. Julien, E. Knobloch, J. Werne, Numerical simulation of an asymptotically reduced system for rotationally constrained convection, J. Fluid Mech. 551 (2006) 141–174.
[56] K. Julien, E. Knobloch, A.M. Rubio, G.M. Vasil, Heat transport in low-Rossby-number Rayleigh–Bénard convection, Phys. Rev. Lett. 109 (2012) 254503.
[57] M. Plumley, K. Julien, P. Marti, S. Stellmach, Sensitivity of rapidly rotating Rayleigh–Bénard convection to Ekman pumping, Phys. Rev. Fluids 2 (2017) 094801.
[58] N. Gillet, C.A. Jones, The quasi-geostrophic model for rapidly rotating spherical convection outside the tangent cylinder, J. Fluid Mech. 554 (2006) 343–369.
[59] M. Madonia, A.J.A. Guzmán, H.J.H. Clercx, R.P.J. Kunnen, Reynolds number scaling and energy spectra in geostrophic convection, J. Fluid Mech. 962 (2023) A36.
[60] E.K. Hawkins, J.S. Cheng, J.A. Abbate, T. Pilegard, S. Stellmach, K. Julien, J.M. Aurnou, Laboratory models of planetary core-style convective turbulence, Fluids 8 (2023) 106.
[61] R. Verzicco, P. Orlandi, A finite-difference scheme for three-dimensional incompressible flows in cylindrical coordinates, J. Comput. Phys. 123 (1996) 402–414.

[62] E.P. van der Poel, R. Ostilla-Mónico, J. Donners, R. Verzicco, A pencil distributed finite difference code for strongly turbulent wall-bounded flows, Comput. & Fluids 116 (2015) 10–16.
[63] X. Zhu, E. Phillips, V. Spandan, J. Donners, G. Ruetsch, J. Romero, R. Ostilla-Mónico, Y. Yang, D. Lohse, R. Verzicco, M. Fatica, R.J. Stevens, AFiD-GPU: A versatile Navier–Stokes solver for wall-bounded turbulent flows on GPU clusters, Comp. Phys. Commu. 229 (2018) 199–210.
[64] R. Verzicco, R. Camussi, Numerical experiments on strongly turbulent thermal convection in a slender cylindrical cell, J. Fluid Mech. 477 (2003) 19–49.
[65] O. Shishkina, R.J.A.M. Stevens, S. Grossmann, D. Lohse, Boundary layer structure in turbulent thermal convection and its consequences for the required numerical resolution, New J. Phys. 12 (2010) 075022.
[66] X.M. de Wit, A.J.A. Guzmán, H.J.H. Clercx, R.P.J. Kunnen, Discontinuous transitions towards vortex condensates in buoyancy-driven rotating turbulence, J. Fluid Mech. 936 (2022) A43.
[67] R.P.J. Kunnen, R.J.A.M. Stevens, J. Overkamp, C. Sun, G.F. van Heijst, H.J.H. Clercx, The role of Stewartson and Ekman layers in turbulent rotating Rayleigh–Bénard convection, J. Fluid Mech. 688 (2011) 422–442.
[68] R.P.J. Kunnen, R. Ostilla-Mónico, E.P. van der Poel, R. Verzicco, D. Lohse, Transition to geostrophic convection: the role of the boundary conditions, J. Fluid Mech. 799 (2016) 413–432.
[69] J. Shi, H. Lu, S. Ding, J. Zhong, Fine vortex structure and flow transition to the geostrophic regime in rotating Rayleigh–Bénard convection, Phys. Rev. Fluids 65 (2020) 011501.
[70] R.E. Ecke, X. Zhang, O. Shishkina, Connecting wall modes and boundary zonal flows in rotating Rayleigh–Bénard convection, Phys. Rev. Fluids 7 (2022) L011501.
[71] X. Zhang, P. Reiter, O. Shishkina, R.E. Ecke, Wall modes and the transition to bulk convection in rotating Rayleigh–Bénard convection, Phys. Rev. Fluids 9 (2024) 053501.
[72] P. Wei, S. Weiss, G. Ahlers, Multiple transitions in rotating turbulent Rayleigh–Bénard convection, Phys. Rev. Lett. 114 (2015) 114506.
[73] J.-Q. Zhong, R.J.A.M. Stevens, H.J.H. Clercx, R. Verzicco, D. Lohse, G. Ahlers, Prandtl-, Rayleigh-, and Rossby-number dependence of heat transport in turbulent rotating Rayleigh–Bénard convection, Phys. Rev. Lett. 102 (2009) 044502.
[74] R.J.A.M. Stevens, H.J.H. Clercx, D. Lohse, Heat transport and flow structure in rotating Rayleigh–Bénard convection, Eur. J. Mech. 40 (2013) 41–49.
[75] D. Nieves, A.M. Rubio, K. Julien, Statistical classification of flow morphology in rapidly rotating Rayleigh–Bénard convection, Phys. Fluids 26 (2014) 086602.
[76] T.G. Oliver, A.S. Jacobi, K. Julien, M.A. Calkins, Small scale quasigeostrophic convective turbulence at large Rayleigh number, Phys. Rev. Fluids 8 (2023) 093502.
[77] A.J.A. Guzmán, M. Madonia, J.S. Cheng, R. Ostilla-Mónico, H.J.H. Clercx, R.P.J. Kunnen, Flow- and temperature-based statistics characterizing the regimes in rapidly rotating turbulent convection in simulations employing no-slip boundary conditions, Phys. Rev. Fluids 7 (1) (2022) 013501.
[78] D. Lohse, O. Shishkina, Ultimate turbulent thermal convection, Phys. Today 76 (2023) 26–32.
[79] T. Gastine, J. Wicht, J. Aubert, Scaling regimes in spherical shell rotating convection, J. Fluid Mech. 808 (2016) 690–732.
[80] D.J. Stevenson, Turbulent thermal convection in the presence of rotation and a magnetic field – a heuristic theory, Geophys. Astrophys. Fluid Dyn. 12 (1979) 139–169.
[81] R.P.J. Kunnen, B.J. Geurts, H.J.H. Clercx, Experimental and numerical investigation of turbulent convection in a rotating cylinder, J. Fluid Mech. 642 (2010) 445–476.
[82] Y. Liu, R.E. Ecke, Local temperature measurements in turbulent rotating Rayleigh–Bénard convection, Phys. Rev. E. 84 (2011) 016311.
[83] R. Verzicco, R. Camussi, Prandtl number effects in convective turbulence, J. Fluid Mech. 383 (1999) 55–473.
[84] M. Breuer, S. Wessling, J. Schmalzl, U. Hansen, Effect of inertia in Rayleigh–Bénard convection, Phys. Rev. E 69 (2004) 026302.
[85] C. Guervilly, D.W. Hughes, C.A. Jones, Large-scale vortices in rapidly rotating Rayleigh–Bénard convection, J. Fluid Mech. 758 (2014) 407–435.
[86] S. Grossmann, D. Lohse, Thermal convection for large Prandtl numbers, Phys. Rev. Lett. 86 (2001) 3316.
[87] A. Teimurazov, M. McCormack, M. Linkmann, O. Shishkina, Unifying heat transport model for the transition between buoyancy-dominated and Lorentz-force-dominated regimes in quasistatic magnetoconvection, J. Fluid Mech. 980 (2024) R3.
[88] E.M. King, J.M. Aurnou, Turbulent convection in liquid metal with and without rotation, Proc. Natl. Acad. Sci. USA 110 (2013) 17.